iScience

CellPress
OPEN ACCESS

Article

Anode-Driven Controlled Release of Cathodic Fuel via pH Response for Smart Enzymatic Biofuel Cell

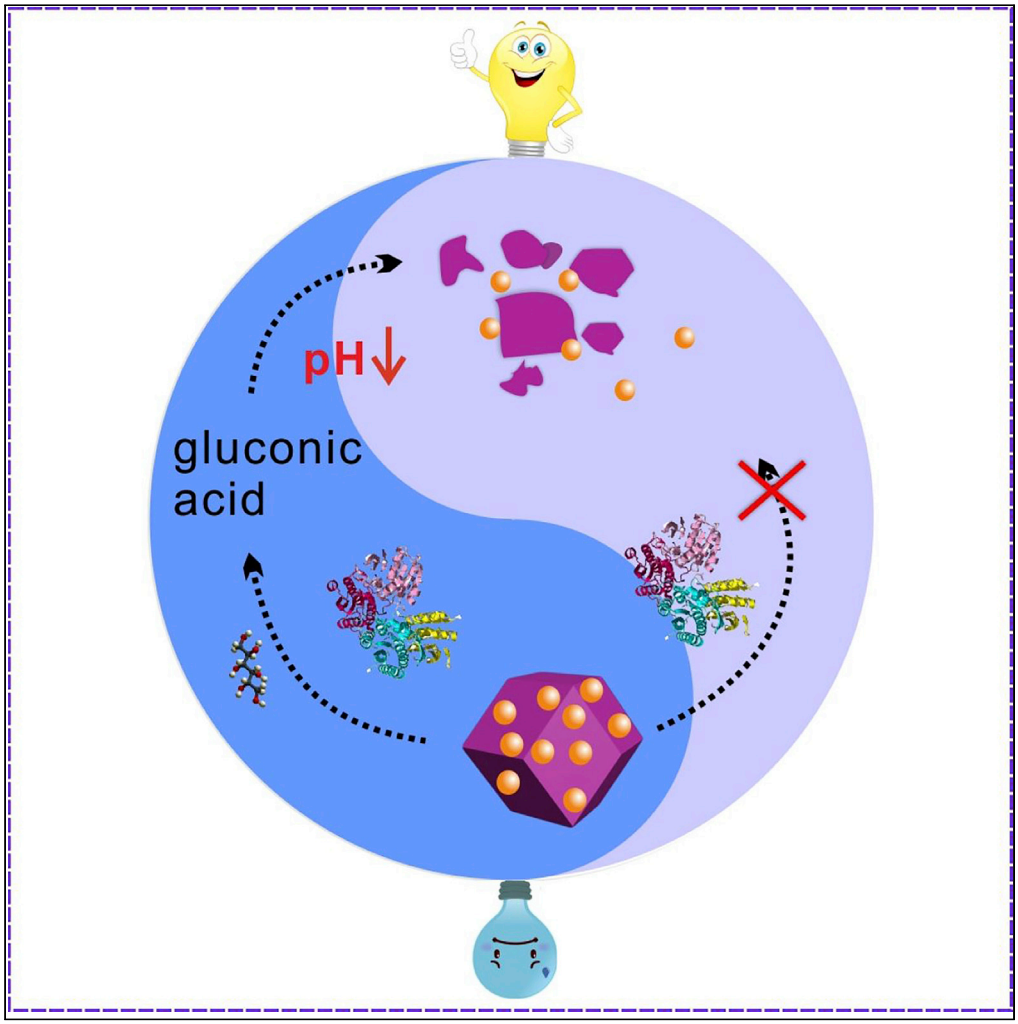

Panpan Gai, Chengcheng Gu, Xinke Kong, Feng Li

lifeng@qau.edu.cn

HIGHLIGHTS

A smart membrane-less enzymatic biofuel cell was fabricated

Anode-driven controlled cathodic acceptor release was engineered by pH-responsive nanocarriers

The pH-responsive strategy was realized based on $[Fe(CN)_6]^{3-}$@ZIF-8 nanocarriers

Gai et al., iScience *23*, 101133
June 26, 2020
https://doi.org/10.1016/j.isci.2020.101133

iScience

CellPress
OPEN ACCESS

Article

Anode-Driven Controlled Release of Cathodic Fuel via pH Response for Smart Enzymatic Biofuel Cell

Panpan Gai,[1,2] Chengcheng Gu,[1,2] Xinke Kong,[1] and Feng Li[1,3,*]

SUMMARY

Enzymatic biofuel cells (EBFCs) with or without a membrane to separate the anodic and cathodic compartments generally suffered from high internal resistance or interactive interference, both of which restricted the improvement of their performance. Herein, a smart membrane-less EBFC was engineered based on anode-driven controlled release of cathodic acceptor via pH-responsive metal-organic framework ($[Fe(CN)_6]^{3-}$@ZIF-8) nanocarriers. The glucose anodic oxidation would produce gluconic acid accompanied by the change in pH value from neutral to the acidic case, which could drive the degradation of $[Fe(CN)_6]^{3-}$@-ZIF-8 nanocarriers and further realize the controlled release of cathodic acceptor $[Fe(CN)_6]^{3-}$. More importantly, compared with controlled EBFC with or without membrane, the power output of the as-proposed EBFC enhanced at least 700 times due to the seamless electronic communication. Therefore, the ingenious strategy not only realized the successful engineering of the membrane-less EBFC but also provided an appealing idea for constructing smart devices.

INTRODUCTION

Enzymatic biofuel cells (EBFCs) can convert bioenergy from biochemical reactions directly to electricity and have been widely employed in self-powered biosensors, wearable devices, and implantable power sources (Chen et al., 2019b; Katz and MacVittie, 2013; Miyake et al., 2011; Wu et al., 2017; Xiao et al., 2019). To date, great efforts have been devoted to improving the performance of the EBFC (Fritea et al., 2019; Hickey et al., 2013; Tang et al., 2019). However, a vast majority of them suffered from the long-term coexistence of both anodic and cathodic fuels, which may be prone to interactive interference and the insufficient utilization of biofuels. To address this issue, the membrane was usually introduced to separate the anodic and cathodic chamber (Gai et al., 2016; Gu et al., 2019; Li et al., 2020b; Lv et al., 2018). However, this type of EBFC generally suffered from high internal resistance and lower performance. Even more importantly, it could be not in favor of easy miniaturization platforms or flexible and implantable systems. Thus, it is an urgent demand to develop a new efficient and universal approach for constructing the membrane-less EBFC.

The nanocarrier-controlled release strategy had been widely applied in drug delivery system (Mao et al., 2018; Yang et al., 2019b; Zhang et al., 2016), inspired by which, exploring a suitable nanocarrier would be the critical factor for engineering a smart biofuel cell. Metal-organic frameworks (MOFs) have aroused considerable interest on account of their characteristics of internal volumes and tunable framework chemistries, which exhibited extensive applications in catalysis (Hu et al., 2016; Ma et al., 2014; Wang et al., 2020; Xia et al., 2015; Yang et al., 2019a; Zhang et al., 2014) dynamic therapy (Chen et al., 2018; Lu et al., 2015; Zhang et al., 2018; Zhu et al., 2018), sensing (Chen et al., 2019a; Hu et al., 2017; Kreno et al., 2011; Li et al., 2020a; Ma et al., 2013), as well as drug delivery (Cai et al., 2015; Nazari et al., 2016; Zhao et al., 2016; Zheng et al., 2016). As the typical material, zeolitic imidazolate frameworks 8 (ZIF-8) consisted of Zn^{2+} ions and 2-methylimidazolate ligand had the unique feature of high stability under the neutral physiological condition but easy to degrade under the acidic condition (Lyu et al., 2014; Mao et al., 2018; Pan et al., 2018; Wang et al., 2017; Yang et al., 2019b; Zheng et al., 2017). For example, Willner et al. utilized the ZIF-8 MOFs as the pH-responsive nanocarriers to realize the controlled release of drugs (Chen et al., 2018; Zheng et al., 2016). Generally, in the anode of the EBFC, glucose could be oxidized to gluconic acid accompanied by the change in pH value from neutral to the acidic case (Katz and Pita, 2009). Thus, ZIF-8 could be an excellent nanocarrier in the controlled-release system based on the glucose oxidation in the anode.

[1]College of Chemistry and Pharmaceutical Sciences, Qingdao Agricultural University, Qingdao 266109, P. R. China

[2]These authors contributed equally

[3]Lead Contact

*Correspondence: lifeng@qau.edu.cn

https://doi.org/10.1016/j.isci.2020.101133

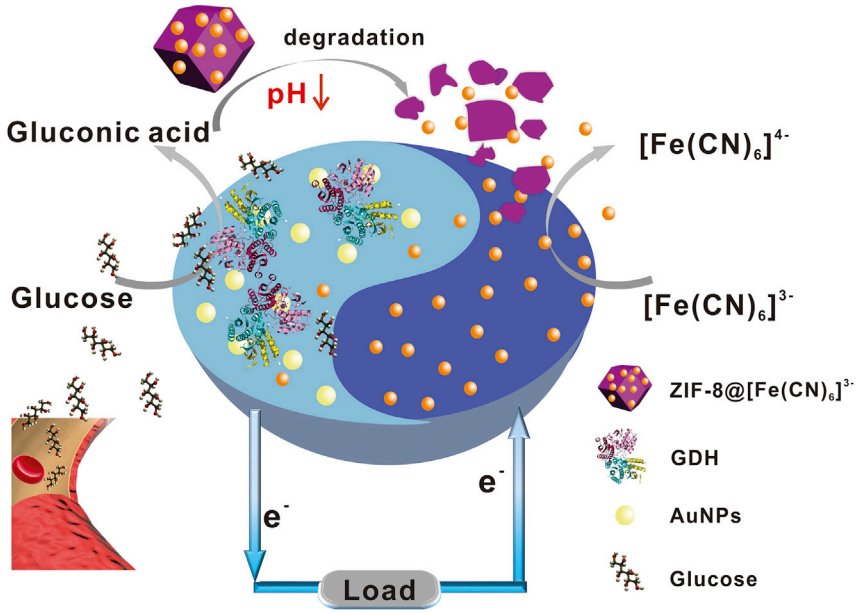

Scheme 1. Schematic Illustration of the Engineering of Smart EBFC Based on Anode-Driven Cathodic Fuel Release via pH-Responsive ZIF-8 Nanocarriers

In this context, a smart membrane-less EBFC was engineered based on the anode-driven controlled release of cathodic fuel via pH-responsive ZIF-8 nanocarriers. As shown in Scheme 1, the EBFC was composed of the positively charged cathode and the glucose dehydrogenase/gold nanoparticles (GDH/AuNPs) anode. Initially, in the absence of glucose, the cathodic acceptor $[Fe(CN)_6]^{3-}$ was encapsulated in ZIF-8 nanocarriers via a one-pot preparation method, thereby leading to a relatively low power output of EBFC. Once glucose was introduced, the GDH-catalyzed anodic oxidation of glucose produced gluconic acid accompanied by the change in pH value from neutral to the acidic case, which drove the degradation of $[Fe(CN)_6]^{3-}$@ZIF-8 nanocarriers and further caused the release of cathodic acceptor $[Fe(CN)_6]^{3-}$ into the electrolyte. Owing to the electrostatic absorption, $[Fe(CN)_6]^{3-}$ diffused to the positively charged cathode surface and accepted the electrons generated from the anode to realize the $[Fe(CN)_6]^{3-}$ reduction (Equation S1), producing a significantly enhanced power output. Therefore, the smart membrane-less EBFC was realized based on the pH-responsive ZIF-8 nanocarriers. Compared with devices with or without membrane, the power output of the as-proposed EBFCs enhanced at least 700 times due to the elaborate engineering of EBFCs. This ingenious strategy not only avoided long-term coexistence of anodic and cathodic fuels but also efficiently improved the performance of EBFCs, which provided an appealing idea for constructing smart devices.

RESULTS AND DISCUSSION

Characterization of the Anode-Driven System

As the starting switch of the EBFC, the catalytic ability of the anode could be a key factor for the performance of EBFC. Accordingly, AuNPs featured with uniform morphology (transmission electron microscopy [TEM] image in Figure S1) were selected as the substrate materials because of their good biocompatibility and excellent conductivity. Furthermore, electrochemical impedance spectroscopy was employed to investigate the stepwise assembly process of the anode in Figure 1A. The charge-transfer resistance (R_{ct}, 60 Ω) of the AuNPs modified electrode was smaller than that of the bare indium tin oxide electrode (108 Ω) due to the excellent conductivity of AuNPs. When GDH was immobilized onto the AuNPs surface, the R_{ct} sharply increased, being attributed to the fact that the non-electroactive GDH protein shell hindered the redox probes from approaching the electrode surface. Afterward, cyclic voltammetries were performed to study the bioelectrocatalytic behavior of the GDH/AuNPs anode in Figures 1B and S2. The onset potential of the glucose oxidation was about −0.1 V. Furthermore, with the addition of glucose, the oxidation current intensity gradually increased, verifying the efficient glucose oxidation. As a deletional control

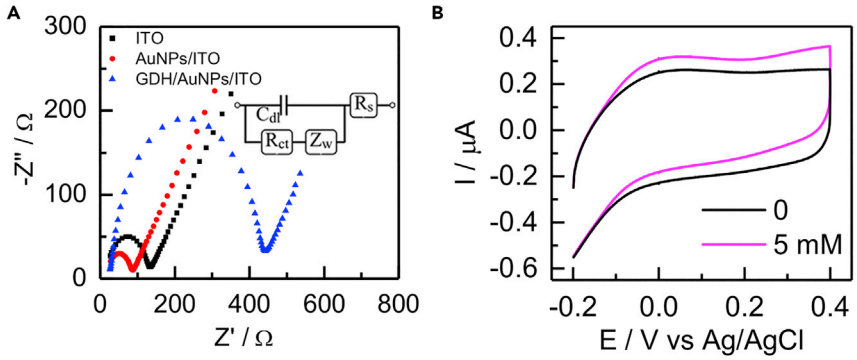

Figure 1. Study of the Anode

(A) Electrochemical impedance spectroscopy of the GDH/AuNPs/ITO anode assembly process.

(B) Cyclic voltammetries of the GDH/AuNPs/ITO anode in 10 mM NaCl solution (pH 7.4) with different glucose concentrations.

experiment, the AuNPs had no catalytic current for glucose oxidation in Figure S3. These results demonstrated that the GDH/AuNPs anode with excellent electrochemical performance was successfully fabricated, further confirming the feasibility of the EBFCs launched by the anode.

Synthesis and Characterization of $[Fe(CN)_6]^{3-}$@ZIF-8 Nanocarriers

$[Fe(CN)_6]^{3-}$@ZIF-8 nanocarriers played a crucial role in the construction of EBFC. Recently, the one-pot method to synthesize organic molecules and proteins encapsulated in ZIFs has been widely studied (Lyu et al., 2014; Zheng et al., 2016). Herein, $[Fe(CN)_6]^{3-}$@ZIF-8 was also synthesized by a one-pot manipulation by adding $[Fe(CN)_6]^{3-}$ into the solution of 2-methylimidazole and zinc acetate, which can overcome the traditional drawbacks of tedious multistep procedures and serious leakage. To validate the successful preparation and explore the properties of $[Fe(CN)_6]^{3-}$@ZIF-8 nanocarriers, a series of characterizations were conducted as follows. First, the X-ray diffraction patterns of the $[Fe(CN)_6]^{3-}$@ZIF-8 were almost in accordance with those of the measured patterns of the pure ZIF-8 ($5° < 2\theta < 30°$), illustrating that the encapsulation of $[Fe(CN)_6]^{3-}$ had negligible effects on the phase of ZIF-8 hosts (Figure 2A). Also, the energy-dispersive spectroscopy results displayed a clear distribution of Fe, Zn, N, and C elements and the atomic content of Fe was 0.59%, which suggested that Fe element originated from cathodic acceptor $[Fe(CN)_6]^{3-}$ was involved in the ZIF-8 nanocarrier (Figure 2B). In addition, TEM showed that the $[Fe(CN)_6]^{3-}$@ZIF-8 basically maintained the rhombic dodecahedral structures similar to pure ZIF-8 with the average particle size of about 150–200 nm (Figures 2C and 2D), demonstrating that the introduction of $[Fe(CN)_6]^{3-}$ had almost no effect on the synthesis of ZIF-8. What's more, TEM images displayed that the morphology of $[Fe(CN)_6]^{3-}$@-ZIF-8 changed negligibly after 2 days at pH 7.4, suggesting the long-term stability under the neutral condition (Figure 2E). The above-mentioned results demonstrated that the as-proposed $[Fe(CN)_6]^{3-}$@ZIF-8 was successfully constructed by a one-pot method, and exhibited excellent long-term stability under the neutral condition.

Feasibility of the Anode-Driven EBFC

ZIF-8 is pH sensitive and easy to degrade under the acidic condition (Chen et al., 2018). To verify whether $[Fe(CN)_6]^{3-}$@ZIF-8 has the same properties, differential pulse voltammetry (DPV) was performed to measure the electrochemical signal of $[Fe(CN)_6]^{3-}$ that was released from $[Fe(CN)_6]^{3-}$@ZIF-8 at different pH values. The current responses presented a negative correlation with the pH values ranging from 4.0 to 7.4 (Figure 3A), illustrating that the release of $[Fe(CN)_6]^{3-}$ could be well controlled by adjusting pH. The negligible variation of the peak current at pH 7.4 and the stability of $[Fe(CN)_6]^{3-}$@ZIF-8 structure under the neutral condition (Figure 2E) verified that $[Fe(CN)_6]^{3-}$ was almost no leak from the nanocarrier. When the $[Fe(CN)_6]^{3-}$@-ZIF-8 was treated at pH 4.0, the peak current of $[Fe(CN)_6]^{3-}$ had a high value due to the efficient degradation of the nanocarriers, which also could be confirmed by the TEM image (Figure 3D). To realize the pH variation, the GDH-catalyzed anodic oxidation of glucose with different concentrations was performed. As expected, with the addition of glucose concentration, the pH value decreased and reached a plateau when the glucose was up to 50 mM (Figures 3B and S4). Furthermore, the relationship between DPV current values and different glucose concentrations was studied in Figure 3C. It can be seen that the DPV current

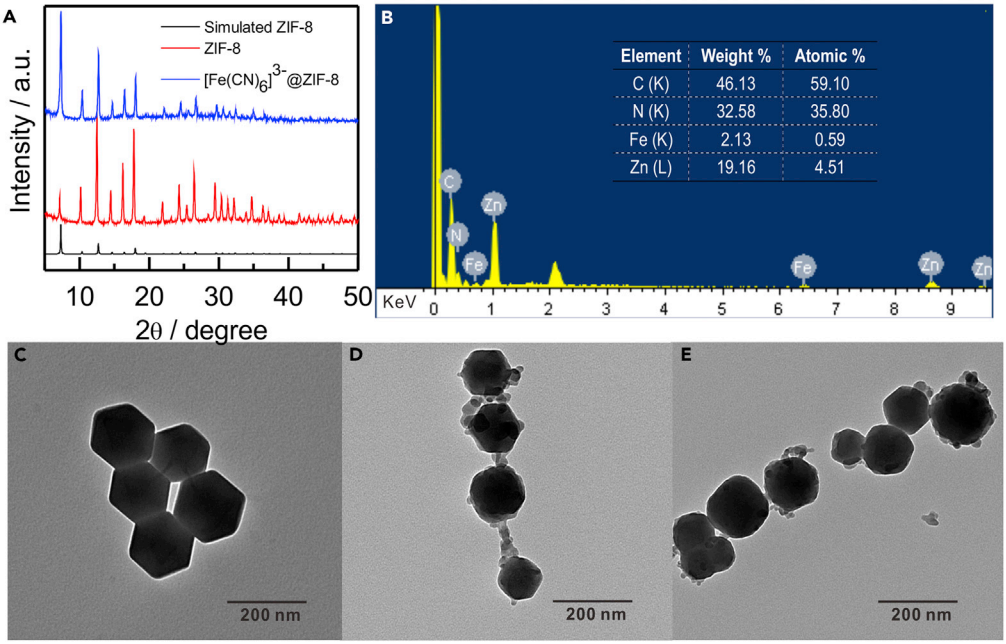

Figure 2. Study of the $[Fe(CN)_6]^{3-}$@ZIF-8

(A) X-ray diffraction patterns of ZIF-8 and $[Fe(CN)_6]^{3-}$@ZIF-8.

(B and C) (B) Energy-dispersive spectrum and elemental percentage of $[Fe(CN)_6]^{3-}$@ZIF-8. TEM images corresponding to (C) pure ZIF-8.

(D) $[Fe(CN)_6]^{3-}$@ZIF-8.

(E) $[Fe(CN)_6]^{3-}$@ZIF-8 storage for 2 days in 10 mM NaCl solution (pH 7.4).

value of $[Fe(CN)_6]^{3-}$ gradually increased with the increase of glucose concentration. Thus, the above-mentioned results strongly verified that the acidic cases caused by glucose oxidation would enable the controlled release of the cathodic acceptor $[Fe(CN)_6]^{3-}$. In the presence of 50 mM glucose, the release amount of $[Fe(CN)_6]^{3-}$ was calculated to be 58.5 μM from the DPV linear equation of standard $[Fe(CN)_6]^{3-}$ (Figure S5). Meanwhile, the effect of glucose concentration on the structure of $[Fe(CN)_6]^{3-}$@ZIF-8 could also be validated by TEM images. As more glucose was introduced, the frame structure of ZIF-8 was damaged more seriously (Figures 3E and 3F), which also well agreed with the current response of $[Fe(CN)_6]^{3-}$. Overall, the anodic biocatalysis could efficiently regulate the concentration variation of the cathodic acceptor. In addition, the current value of $[Fe(CN)_6]^{3-}$ could retain its original signal in the presence or absence of glucose at intervals of 4 days for 20 days, which implied the excellent stability of $[Fe(CN)_6]^{3-}$@ZIF-8 (Figure S6). All the results laid a solid foundation for constructing the anode-driven membrane-less EBFC with excellent performance.

Optimization of $[Fe(CN)_6]^{3-}$@ZIF-8 Nanocarriers

The optimization for $[Fe(CN)_6]^{3-}$@ZIF-8 nanocarriers was carried out to maximize the performance of the EBFC, including the concentration and the release time of $[Fe(CN)_6]^{3-}$. First, the concentration of the $[Fe(CN)_6]^{3-}$ in $[Fe(CN)_6]^{3-}$@ZIF-8 preparation process was investigated. As depicted in Figure S7A, the peak current increased with increasing concentrations of $[Fe(CN)_6]^{3-}$ and tended to level off when the concentration was higher than 3 mM, which suggested that ZIF-8 had a certain loading capacity and reached saturation at $[Fe(CN)_6]^{3-}$ concentration of 3 mM. Besides, the effect of the $[Fe(CN)_6]^{3-}$ release time was examined to ensure the complete degradation of the nanocarriers. Figure S7B showed that a maximum peak current was obtained up to 3 min, and it barely changed with an even much longer time, indicating that $[Fe(CN)_6]^{3-}$@ZIF-8 could be completely destroyed in 3 min. Hence, 3 min was chosen as the optimal release time.

Anode-Driven Signal Response of EBFC

Based on the above-mentioned analysis, the polarization curves (Figure 4A) and power output curves (Figure 4B) of the anode-driven EBFC with different glucose concentrations were obtained. The results

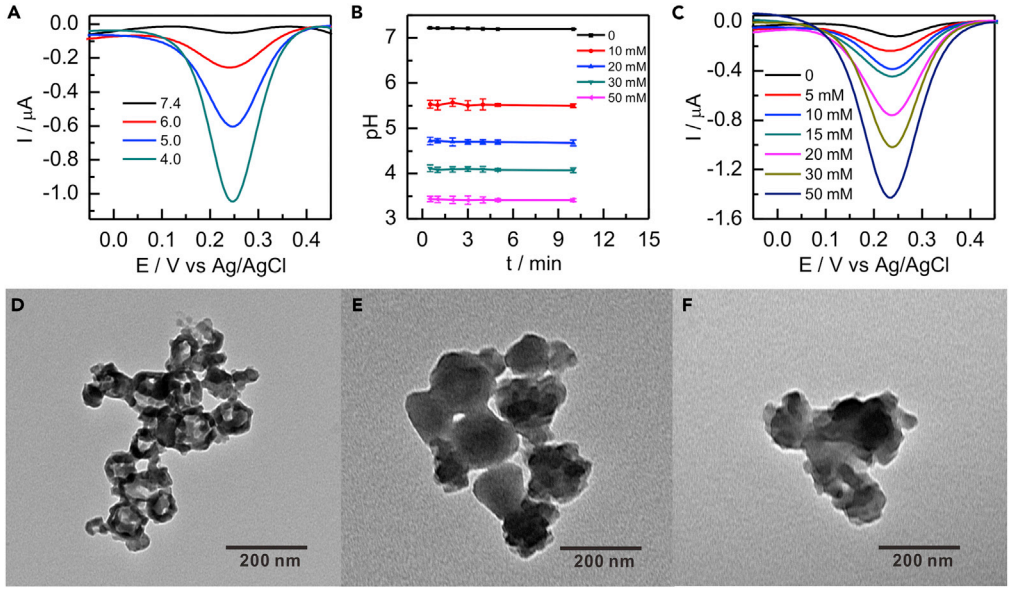

Figure 3. Study of the $[Fe(CN)_6]^{3-}$@ZIF-8 Under Different Conditions

(A) DPVs of the $[Fe(CN)_6]^{3-}$@ZIF-8 under different pH values.

(B) pH value variation induced by the GDH-catalyzed anodic oxidation of glucose with different concentrations. Error bars represent the standard deviation of three independent measurments.

(C–F) (C) DPVs of the $[Fe(CN)_6]^{3-}$@ZIF-8 under different glucose concentrations. TEM images of the $[Fe(CN)_6]^{3-}$@ZIF-8 after treatment with 10 mM NaCl solution (pH 4.0) (D) and 5 mM (E) and 50 mM (F) glucose for 30 min, respectively.

displayed that the open-circuit voltage (E^{OCV}) and the maximum power output (P_{max}) of the EBFC showed a positive correlation with the glucose concentration. When the glucose concentration was 50 mM, the E^{OCV} and P_{max} reached 0.38 V and 23 μW cm^{-2}, respectively. The internal resistance of EBFC was calculated about 5,790 Ω by $P_{max} = I^2R$. To confirm the superior performance of the anode-driven EBFC, a series of deletional control experiments were carried out, in which the EBFCs with or without the membrane were fabricated at the same concentrations of glucose (50 mM) and $[Fe(CN)_6]^{3-}$ (58.5 μM). The E^{OCV} and P_{max} of the membrane EBFCs were 0.15 V and 0.03 μW cm^{-2}, respectively (Figure S8A), which was much lower than that of the as-proposed EBFC. It might be caused by the high internal resistance of 18,750 Ω originating from the membrane. For the traditional membrane-less EBFCs, the E^{OCV} (7.5 mV) and P_{max} (0.07 nW cm^{-2}) were almost negligible (Figure S8B), which was attributed to the fact that there are interferences between the anodic biofuel (glucose) and the cathodic biofuel ($[Fe(CN)_6]^{3-}$). In contrast, the as-proposed EBFC could avoid the interactive interference of the biofuels and enhance the electrical communication between the anode and cathode due to the presence of $[Fe(CN)_6]^{3-}$@ZIF-8 nanocarriers. In addition, the excellent performance of the anode-driven EBFC for different glucose concentrations would also broaden the applications in self-powered glucose biosensors. Herein, the glucose response in as-proposed self-powered biosensors was shown in Figure S9, the linear regression equation was $P_{max}/\mu W \cdot cm^{-2} = 0.374[glucose] + 5.640$ ($R^2 = 0.983$) with detection limit of 1.6 mM ($3\sigma/k$, where σ is the standard deviation of the blank sample and k is the slope of the analytical calibration). Thus the ingenious EBFC-based self-powered glucose biosensors would be a robust alternative choice for the point-of-care diagnosis.

Selectivity and Stability of the Anode-Driven EBFC

The specificity of the EBFC was tested by using other three saccharides such as fructose, maltose, and lactose. As depicted in Figure 4C, the interferences with the same concentration showed no obvious signal response compared with glucose, which manifested the good selectivity of the EBFC. Moreover, the long-term stability of the EBFC was also investigated by measuring the P_{max} response in the absence and presence of 50 mM glucose every 4 days. It was found that whether the glucose was present or not, EBFC still nearly maintained its original signal in the continuous tests (Figure 4D), demonstrating that the anode-driven EBFC featured with excellent stability.

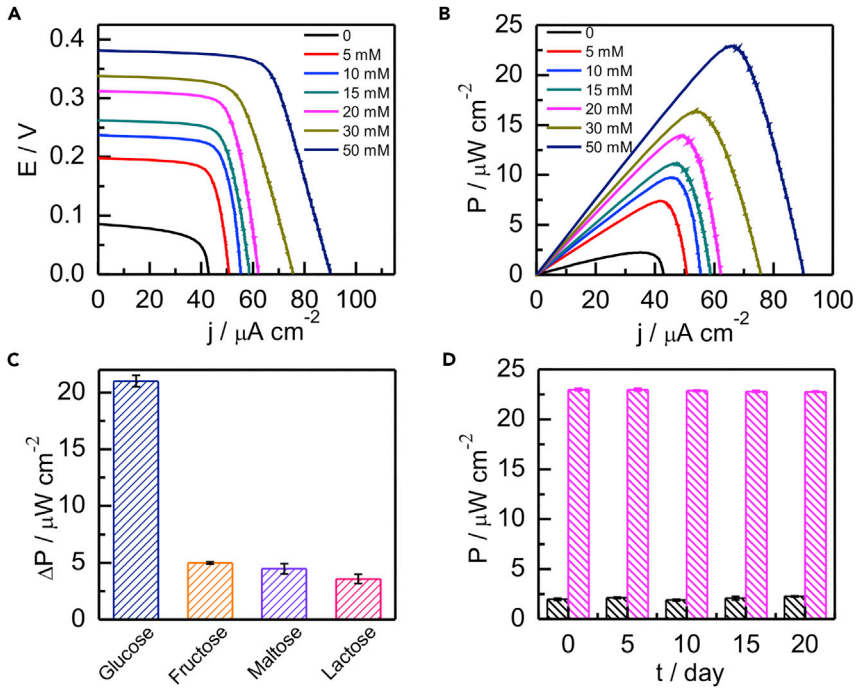

Figure 4. Investigation of the Anode-Driven EBFC

(A) Polarization curves.

(B) Power output curves of the anode-driven EBFC response with different concentrations of glucose.

(C) The selectivity of the anode-driven EBFC in the presence of 50 mM saccharides. $\Delta P = P - P_0$, in which P_0 was the blank signal of EBFC in the absence of saccharides. Error bars represent the standard deviation of three independent measurements.

(D) Stability analysis of the anode-driven EBFC in the presence and absence of 50 mM glucose in 20 days. Error bars represent the standard deviation of three independent measurements.

Conclusion

In summary, a smart membrane-less EBFC was engineered by fully taking advantage of pH-sensitive properties of ZIF-8 and the anodic oxidation of glucose to gluconic acid. Encouragingly, the as-proposed anode-driven cathodic acceptor release system not only significantly decreased the internal resistance but also realized the seamless electronic communication between the anode and cathode. Compared with EBFC with or without membrane in the same conditions, the power output of the anode-driven EBFC enhanced at least 700 times. Overall, the as-proposed strategy provides a brand new idea for the construction of EBFC with high performance and pushes forward the development of smart devices.

Limitations of the Study

Although the smart membrane-less EBFC here was realized based on the pH-responsive ZIF-8 nanocarriers here, the other smart strategy needs to be further explored to get the device higher performance output. Besides, in this study, the implantation of EBFC has not been investigated, which requires more detailed studies.

Resource Availability

Lead Contact

Feng Li lifeng@qau.edu.cn.

Materials Availability

Our study did not generate any new unique reagents.

Data and Code Availability

Our study did not report any unpublished custom code, software, or algorithm.

METHODS

All methods can be found in the accompanying Transparent Methods supplemental file.

SUPPLEMENTAL INFORMATION

Supplemental Information can be found online at https://doi.org/10.1016/j.isci.2020.101133.

ACKNOWLEDGMENTS

We gratefully appreciate the financial support from the National Natural Science Foundation of China (21605092 and 21775082), the Natural Science Foundation of Shandong Province (ZR2019YQ23), Shandong Province Higher Educational Program for Young Innovation Talents, Major Program of Shandong Province Natural Science Foundation (ZR2018ZC0127), the Research Foundation for Distinguished Scholars of Qingdao Agricultural University (663-1117002), and the Special Foundation for Taishan Scholar of Shandong Province (No. ts201511052).

AUTHOR CONTRIBUTIONS

C.G. and X.K. planned and performed the experiments. P.G. and F.L. planned and supervised the experiments. All authors discussed the results and participated in the formulation of the manuscript.

DECLARATION OF INTERESTS

The authors declare no competing interests.

Received: March 16, 2020
Revised: April 14, 2020
Accepted: April 29, 2020
Published: June 26, 2020

REFERENCES

Cai, W., Chu, C.C., Liu, G., and Wang, Y.X. (2015). Metal-organic framework-based nanomedicine platforms for drug delivery and molecular imaging. Small *11*, 4806–4822.

Chen, W.H., Luo, G.F., Vazquez-Gonzalez, M., Cazelles, R., Sohn, Y.S., Nechushtai, R., Mandel, Y., and Willner, I. (2018). Glucose-responsive metal-organic-framework nanoparticles act as "smart" sense-and-treat carriers. ACS Nano *12*, 7538–7545.

Chen, X., Yin, L., Lv, J., Gross, A.J., Le, M., Gutierrez, N.G., Li, Y., Jeerapan, I., Giroud, F., Berezovska, A., et al. (2019a). Stretchable and flexible buckypaper-based lactate biofuel cell for wearable electronics. Adv. Funct. Mater. *29*, 1905785.

Chen, H.F., Bai, Z., Dai, X.Q., Zeng, X.Q., Cano, Z.P., Xie, X.X., Zhao, M.Y., Li, M., Wang, H., Chen, Z.W., et al. (2019b). In situ engineering of intracellular hemoglobin for implantable highperformance biofuel cells. Angew. Chem. Int. Ed. *58*, 6663–6668.

Fritea, L., Gross, A.J., Gorgy, K., O'Reilly, R.K., Le Goff, A., and Cosnier, S. (2019). A bifunctional triblock polynorbornene/carbon nanotube buckypaper bioelectrode for low-potential/high-current thionine-mediated glucose oxidation by FAD-GDH. J. Mater. Chem. A. *7*, 1447–1450.

Gai, P.P., Ji, Y.S., Wang, W.J., Song, R.B., Zhu, C., Chen, Y., Zhang, J.R., and Zhu, J.J. (2016). Ultrasensitive self-powered cytosensor. Nano Energy *19*, 541–549.

Gu, C.C., Kong, X.K., Liu, X.J., Gai, P.P., and Li, F. (2019). Enzymatic biofuel-cell-based self-powered biosensor integrated with DNA amplification strategy for ultrasensitive detection of single-nucleotide polymorphism. Anal. Chem. *91*, 8697–8704.

Hickey, D.P., Giroud, F., Schmidtke, D.W., Glatzhofer, D.T., and Minteer, S.D. (2013). Enzyme cascade for catalyzing sucrose oxidation in a biofuel cell. ACS Catal. *3*, 2729–2737.

Hu, H., Han, L., Yu, M., Wang, Z., and Lou, X.W. (2016). Metal-organic-framework-engaged formation of Co nanoparticle-embedded carbon@Co_9S_8 double-shelled nanocages for efficient oxygen reduction. Energy Environ. Sci. *9*, 107–111.

Hu, Y., Cheng, H., Zhao, X., Wu, J., Muhammad, F., Lin, S., He, J., Zhou, L., Zhang, C., Deng, Y., et al. (2017). Surface-enhanced Raman scattering active gold nanoparticles with enzyme-mimicking activities for measuring glucose and lactate in living tissues. ACS Nano *11*, 5558–5566.

Katz, E., and MacVittie, K. (2013). Implanted biofuel cells operating in vivo – methods, applications and perspectives – feature article. Energy Environ. Sci. *6*, 2791–2803.

Katz, E., and Pita, M. (2009). Biofuel cells controlled by logically processed biochemical signals: towards physiologically regulated bioelectronic devices. Chem. Eur. J. *15*, 12554–12564.

Kreno, L.E., Leong, K., Farha, O.K., Allendorf, M., Van Duyne, R.P., and Hupp, J.T. (2011). Metal–organic framework materials as chemical sensors. Chem. Rev. *112*, 1105–1125.

Li, X., Li, D., Zhang, Y., Lv, P., Feng, Q., and Wei, Q. (2020a). Encapsulation of enzyme by metal-organic framework for single-enzymatic biofuel cell-based self-powered biosensor. Nano Energy *68*, 104308.

Li, X., Lv, P., Yao, Y., Feng, Q., Mensah, A., Li, D., and Wei, Q. (2020b). A novel single-enzymatic biofuel cell based on highly flexible conductive bacterial cellulose electrode utilizing pollutants as fuel. Chem. Eng. J. *379*, 122316.

Lu, K., He, C., and Lin, W. (2015). A chlorin-based nanoscale metal-organic framework for photodynamic therapy of colon cancers. J. Am. Chem. Soc. *137*, 7600–7603.

Lv, P., Zhou, H., Mensah, A., Feng, Q., Wang, D., Hu, X., Cai, Y., Amerigo Lucia, L., Li, D., and Wei, Q. (2018). A highly flexible self-powered biosensor for glucose detection by epitaxial deposition of gold nanoparticles on conductive bacterial cellulose. Chem. Eng. J. *351*, 177–188.

Lyu, F., Zhang, Y., Zare, R.N., Ge, J., and Liu, Z. (2014). One-pot synthesis of protein-embedded metal-organic frameworks with enhanced biological activities. Nano Lett. *14*, 5761–5765.

Ma, W., Jiang, Q., Yu, P., Yang, L., and Mao, L. (2013). Zeolitic imidazolate framework-based electrochemical biosensor for in vivo

electrochemical measurements. Anal. Chem. *85*, 7550–7557.

Ma, T.Y., Dai, S., Jaroniec, M., and Qiao, S.Z. (2014). Metal-organic framework derived hybrid Co_3O_4-carbon porous nanowire arrays as reversible oxygen evolution electrodes. J. Am. Chem. Soc. *136*, 13925–13931.

Mao, D., Hu, F., Kenry, Ji, S., Wu, W., Ding, D., Kong, D., and Liu, B. (2018). Metal-organic-framework-assisted in vivo bacterial metabolic labeling and precise antibacterial therapy. Adv. Mater. *30*, e1706831.

Miyake, T., Haneda, K., Nagai, N., Yatagawa, Y., Onami, H., Yoshino, S., Abe, T., and Nishizawa, M. (2011). Enzymatic biofuel cells designed for direct power generation from biofluids in living organisms. Energy Environ. Sci. *4*, 5008–5012.

Nazari, M., Rubio-Martinez, M., Tobias, G., Barrio, J.P., Babarao, R., Nazari, F., Konstas, K., Muir, B.W., Collins, S.F., Hill, A.J., et al. (2016). Metal-organic-framework-coated optical fibers as light-triggered drug delivery vehicles. Adv. Funct. Mater. *26*, 3244–3249.

Pan, Y., Sun, K., Liu, S., Cao, X., Wu, K., Cheong, W.C., Chen, Z., Wang, Y., Li, Y., Liu, Y., et al. (2018). Core-shell ZIF-8@ZIF-67-derived CoP nanoparticle-embedded N-doped carbon nanotube hollow polyhedron for efficient overall water splitting. J. Am. Chem. Soc. *140*, 2610–2618.

Tang, J., Werchmeister, R.M.L., Preda, L., Huang, W., Zheng, Z., Leimkühler, S., Wollenberger, U., Xiao, X., Engelbrekt, C., Ulstrup, J., and Zhang, J. (2019). Three-dimensional sulfite oxidase bioanodes based on graphene functionalized carbon paper for sulfite/O_2 biofuel cells. ACS Catal. *9*, 6543–6554.

Wang, Q., Zhang, X., Huang, L., Zhang, Z., and Dong, S. (2017). GOx@ZIF-8(NiPd) nanoflower: an artificial enzyme system for tandem catalysis. Angew. Chem. Int. Ed. *56*, 16082–16085.

Wang, Y., Zhao, S., Zhu, Y., Qiu, R., Gengenbach, T., Liu, Y., Zu, L., Mao, H., Wang, H., Tang, J., et al. (2020). Three-dimensional hierarchical porous nanotubes derived from metal-organic frameworks for highly efficient overall water splitting. iScience *23*, 100761.

Wu, F., Yu, P., and Mao, L. (2017). Self-powered electrochemical systems as neurochemical sensors: toward self-triggered in vivo analysis of brain chemistry. Chem. Soc. Rev. *46*, 2692–2704.

Xia, W., Zou, R., An, L., Xia, D., and Guo, S. (2015). A metal–organic framework route to in situ encapsulation of Co@Co_3O_4@C core@bishell nanoparticles into a highly ordered porous carbon matrix for oxygen reduction. Energy Environ. Sci. *8*, 568–576.

Xiao, X., Xia, H.Q., Wu, R., Bai, L., Yan, L., Magner, E., Cosnier, S., Lojou, E., Zhu, Z., and Liu, A. (2019). Tackling the challenges of enzymatic (bio) fuel cells. Chem. Rev. *119*, 9509–9558.

Yang, D.H., Zhou, H.Y., Liu, H., and Han, B.H. (2019a). Hollow N-doped carbon polyhedrons with hierarchically porous shell for confinement of polysulfides in lithium-sulfur batteries. iScience *13*, 243–253.

Yang, X., Tang, Q., Jiang, Y., Zhang, M., Wang, M., and Mao, L. (2019b). Nanoscale ATP-responsive zeolitic imidazole framework-90 as a general platform for cytosolic protein delivery and genome editing. J. Am. Chem. Soc. *141*, 3782–3786.

Zhang, Z., Chen, Y., Xu, X., Zhang, J., Xiang, G., He, W., and Wang, X. (2014). Well-defined metal-organic framework hollow nanocages. Angew. Chem. Int. Ed. *53*, 429–433.

Zhang, P., Wang, C., Zhao, J., Xiao, A., Shen, Q., Li, L., Li, J., Zhang, J., Min, Q., Chen, J., et al. (2016). Near infrared-guided smart nanocarriers for microRNA-controlled release of doxorubicin/siRNA with intracellular ATP as fuel. ACS Nano *10*, 3637–3647.

Zhang, Y., Wang, F., Liu, C., Wang, Z., Kang, L., Huang, Y., Dong, K., Ren, J., and Qu, X. (2018). Nanozyme decorated metal-organic frameworks for enhanced photodynamic therapy. ACS Nano *12*, 651–661.

Zhao, H.X., Zou, Q., Sun, S.K., Yu, C., Zhang, X., Li, R.J., and Fu, Y.Y. (2016). Theranostic metal-organic framework core-shell composites for magnetic resonance imaging and drug delivery. Chem. Sci. *7*, 5294–5301.

Zheng, H., Zhang, Y., Liu, L., Wan, W., Guo, P., Nystrom, A.M., and Zou, X. (2016). One-pot synthesis of metal-organic frameworks with encapsulated target molecules and their applications for controlled drug delivery. J. Am. Chem. Soc. *138*, 962–968.

Zheng, C., Wang, Y., Phua, S.Z.F., Lim, W.Q., and Zhao, Y. (2017). ZnO–Dox@ZIF-8 core–shell nanoparticles for pH-responsive drug delivery. ACS Biomater. Sci. Eng. *3*, 2223–2229.

Zhu, P., Chen, Y., and Shi, J. (2018). Nanoenzyme-augmented cancer sonodynamic therapy by catalytic tumor oxygenation. ACS Nano *12*, 3780–3795.

iScience, Volume *23*

Supplemental Information

Anode-Driven Controlled Release of Cathodic Fuel via pH Response for Smart Enzymatic Biofuel Cell

Panpan Gai, Chengcheng Gu, Xinke Kong, and Feng Li

Supporting Information

Transparent Methods

Materials and Reagents. Flavin adenine dinucleotide (FAD)-depended glucose dehydrogenase (GDH) was purchased from Toyobo Co., Ltd. (Japan). 2-Methylimidazole was obtained from Adamas Reagent Co., Ltd. 1-Ethyl-3-(3-dimethyl-aminopropyl) carbodiimide hydrochloride (EDC), *N*-hydroxysuccinimide (NHS), and 3-triethoxysilylpropylamine (APTES) were all purchased from Sigma-Aldrich (St. Louis, MO, U.S.A.). Zinc acetate and chloroauric acid ($HAuCl_4 \cdot 4H_2O$) were commercially available from Shanghai Chemical Reagent Co., Ltd. (Shanghai, China). β-$_D$-Glucose was obtained from Tokyo Chemical Industry Co., Ltd. (Japan). AuNPs were prepared according to the literature by adding a sodium citrate solution to a boiling $HAuCl_4$ solution.(Li et al. 2010) All reagents were of analytical grade and were used as received without further purification. Ultrapure water (resistivity >18.2 MΩ cm at 25°C) obtained from a Milli-Q water purification system (Millipore Corp, Bedford, MA, U.S.A.) was used for all the experiments.

Apparatus. Transmission electron microscopy (TEM) images were recorded on an HT7700 microscope (Hitachi, Japan) operated at 100 kV. Scanning electron microscopy (SEM)-energy dispersive spectroscopy (EDS) was measured on a JEOL 7500F SEM (Hitachi, Japan). X-ray diffraction (XRD) patterns were recorded from a D8 ADVANCE (Bruker, Germany). Electrochemical impedance spectroscopy (EIS) was carried out on an Autolab PGSTAT 302N electrochemical analyzer (Metrohm Autolab, The Netherlands), in which the frequency range was 0.1 Hz-100 kHz, and the electrolyte solution was 2.5 mM of $[Fe(CN)_6]^{3-}$/$[Fe(CN)_6]^{4-}$ probe solution. Cyclic voltammetry (CV), differential pulse voltammetry (DPV), linear sweep voltammetry (LSV), and the open-circuit voltage (E^{OCV}) of EBFC measurements were performed on a CHI 660E

electrochemical workstation (Shanghai CH Instrument Co., China) using a three-electrode system: the prepared anode or cathode a Pt wire and an Ag/AgCl were used as the working electrode, the counter electrode, the reference electrode, respectively. All experiments were carried out at room temperature (25 ± 1°C).

Synthesis of $[Fe(CN)_6]^{3-}$@ZIF-8. Briefly, 1.4 M of 2-methylimidazole and 50 mM of zinc acetate were dissolved in ultrapure water with stirring gently at room temperature. Then, 3 mM of $[Fe(CN)_6]^{3-}$ was added quickly and stirred for 2 h. During this process, $[Fe(CN)_6]^{3-}$ could be encapsulated in the ZIF-8. Afterwards, the mixture was centrifuged (6000 rpm, 5 min) and washed with ultrapure water at least three times to remove the unloaded $[Fe(CN)_6]^{3-}$. Finally, the obtained $[Fe(CN)_6]^{3-}$@ZIF-8 was resuspended into ultrapure water and stored at 4°C for further use.

Preparation of the Positively Charged Cathode and the GDH/AuNPs Anode. The washed indium tin oxide (ITO) was immersed in 1 mM of APTES solution for 5 h at room temperature. Then excess APTES was rinsed with ultrapure water. After these pretreatment procedures, a positively charged cathode was obtained.(Gai et al. 2017) Meanwhile, 30 μL of the prepared AuNPs (50 nM) was coated on the surface of the ITO electrode and dried at 37°C for 2 h. Subsequently, the substrate electrode was immersed in the solution containing 10 mg mL^{-1} of EDC/NHS for 30 min to activate the carboxyl group of AuNPs. After being rinsed with ultrapure water to eliminate excess EDC and NHS, the activated electrode was incubated with 20 μL of GDH solution at 4°C overnight to obtain the GDH/ AuNPs anode.

Fabrication of EBFC. The anode-driven membrane-less EBFC was constructed by using the GDH/AuNPs anode and the positively charged cathode, and operated at room temperature. The supporting electrolyte was 1 mL of 10 mM NaCl solution (pH 7.4) containing 100 μL of $[Fe(CN)_6]^{3-}$

@ZIF-8. The E^{OCV} of EBFC was tested by connecting the anode and cathode placed in the electrolytic cell. Polarization curves of the EBFC were measured by linear sweep voltammetry starting from the open-circuit value at a scan rate of 10 mV s^{-1}. The relationship of power output and the current was calculated based on the polarization curve by the formula of $P=UI$. The as-proposed EBFC was stored at 4℃ when not in use.

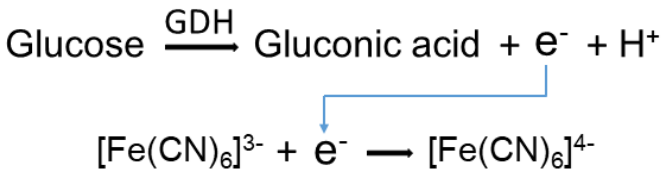

Equation S1. Illustration of the oxidation of glucose and the reduction of $[Fe(CN)_6]^{3-}$, related to Scheme 1.

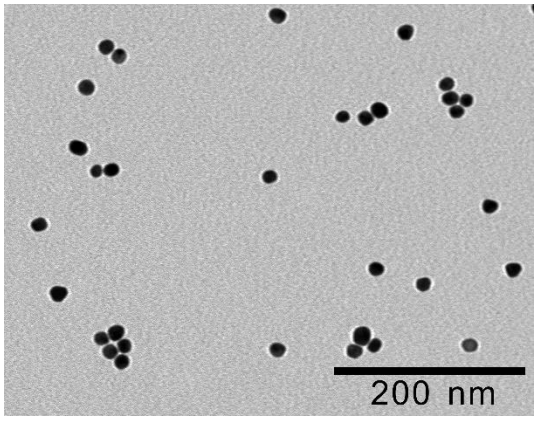

Figure S1. TEM image of AuNPs, related to Figure 1.

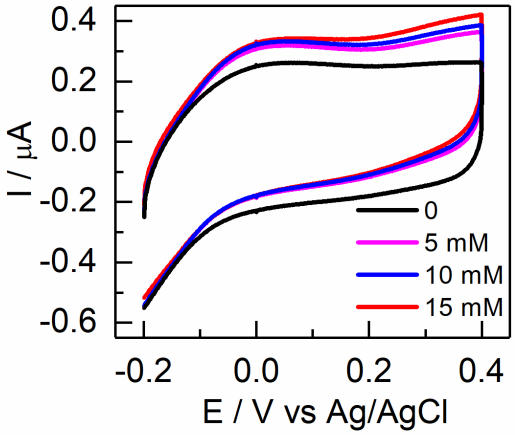

Figure S2. Study of the Anode, related to Figure 1. CVs of the GDH/AuNPs/ITO anode in 10 mM NaCl solution (pH 7.4) with different glucose concentrations.

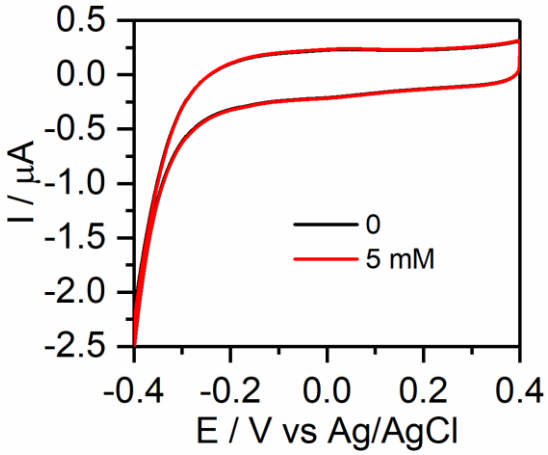

Figure S3. Study of the Anode, related to Figure 1. CVs of the AuNPs/ITO in 10 mM NaCl solution (pH 7.4) with different glucose concentrations.

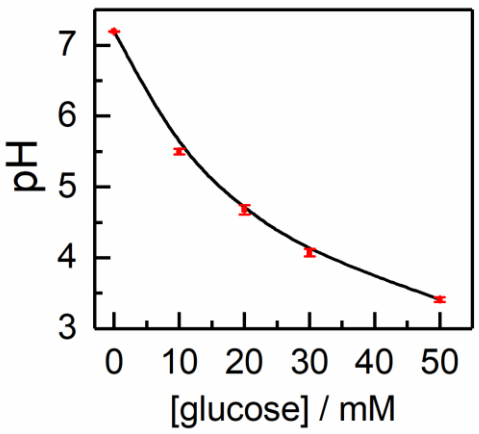

Figure S4. The relationship between pH current values and different glucose concentrations, related to Figure 3. Standard deviation was obtained from three independent measurements.

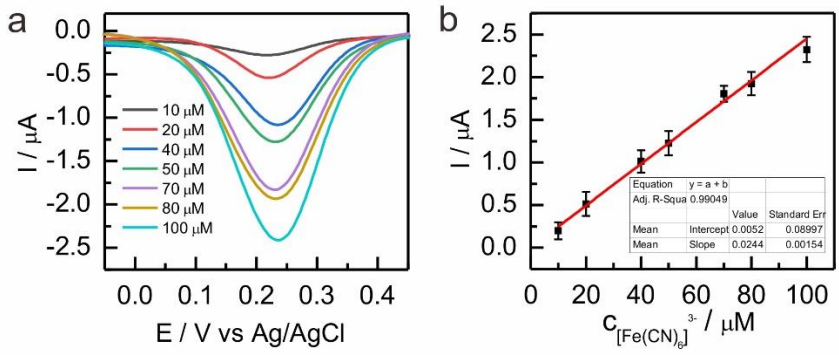

Figure S5. The Relationship Between Current Value and $[Fe(CN)_6]^{3-}$ Concentration, related to Figure 3. (a) DPV curves of the different $[Fe(CN)_6]^{3-}$ concentrations. (b) The linear relationship between current value and $[Fe(CN)_6]^{3-}$ concentration from 10 to 100 μM. Standard deviation was obtained from three independent measurements.

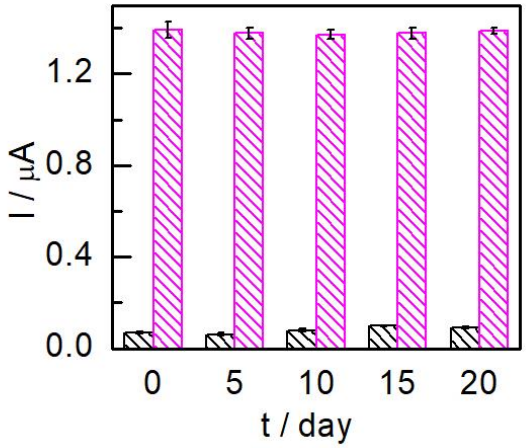

Figure S6. Stability Analysis, related to Figure 3. Stability analysis of the $[Fe(CN)_6]^{3-}$@ZIF-8 nanocarriers in the presence and absence of 50 mM glucose concentration in 20 days. Standard deviation was obtained from three independent measurements.

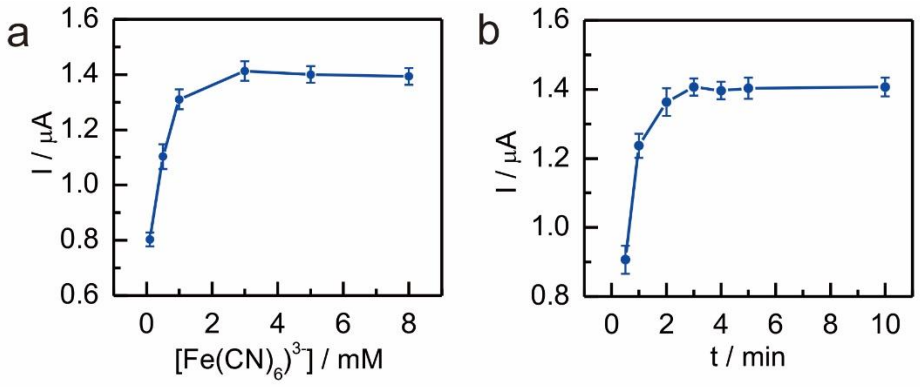

Figure S7. Optimization of $[Fe(CN)_6]^{3-}$ Concentration and the Release Time, related to Figure 3. Effect of (a) $[Fe(CN)_6]^{3-}$ concentration, (b) ZIF-8@$[Fe(CN)_6]^{3-}$ release time. Standard deviation was obtained from three independent measurements.

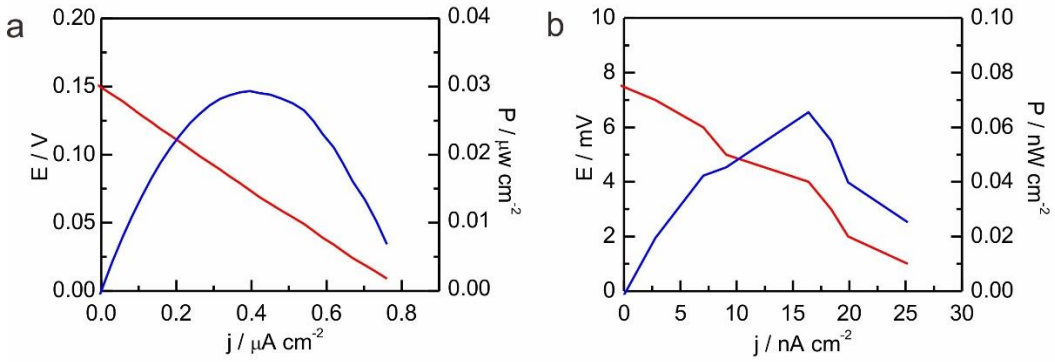

Figure S8. Comparison of Different EBFCs, related to Figure 4. The polarization curves and power output curves of the EBFCs with (a) or without (b) membrane responses with the same concentrations of glucose (50 mM) and $[Fe(CN)_6]^{3-}$ (58.5 μM).

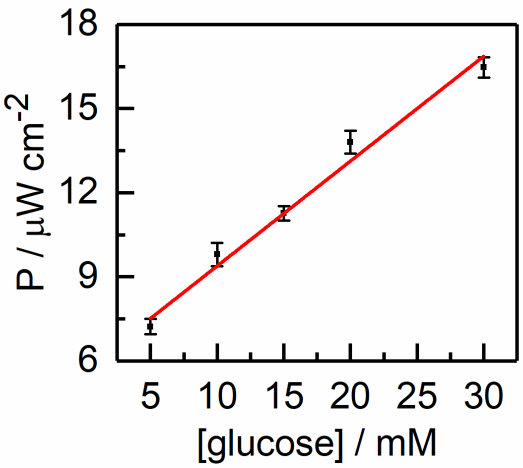

Figure S9. Investigation of the Linear Relationship between Power Output and Glucose Concentration, related to Figure 4. The linear relationship between power output and glucose concentration from 5 to 30 mM. Standard deviation was obtained from three independent measurements.

Gai, P.P., Gu, C.C., Li, H.Y., Sun, X.Z., Li, F. (2017). Ultrasensitive ratiometric homogeneous electrochemical microRNA biosensing via target-triggered Ru(III) release and redox recycling. Anal. Chem. *89*, 12293-12298.

Li, F., Feng, Y., Dong, P., Tang, B. (2010). Gold nanoparticles modified electrode via a mercapto-diazoaminobenzene monolayer and its development in DNA electrochemical biosensor. Biosens. Bioelectron. *25*, 2084-2088.